Mapping Feedback Processes in the Intracluster Medium at low and high redshift

P. Tozzi[1], E. Rasia[2], L. Bassini[2,3], S. Borgani[2,4,5], C. Feruglio[2], R. Gilli[6], A. Liu[1,7], G. Murante[2], L. Pentericci[8], P. Rosati[9], A. Saro[2,4,10], and A. Saxena[8]

[1] INAF – Oss. Astrofisico di Arcetri, largo E. Fermi 5, I-50125 Firenze, Italy, e-mail: `paolo.tozzi@inaf.it`
[2] INAF – Oss. Astronomico di Trieste, Via G.B. Tiepolo 11, I-34131 Trieste, Italy
[3] Center for Theoretical Astrophysics and Cosmology, University of Zurich, Winterthurerstrasse 190, CH-8057 Zürich, Switzerland
[4] Department of Physics, University of Trieste, via Tiepolo 11, I-34131 Trieste, Italy
[5] INFN - National Institute for Nuclear Physics, Via Valerio 2, I-34127 Trieste, Italy
[6] INAF, Oss. di Astrofisica e Scienza dello Spazio, via Piero Gobetti 93/3, I-40129 Bologna, Italy
[7] Max Planck Institute for Extraterrestrial Physics, Giessenbachstrasse 1, 85748 Garching, Germany
[8] INAF - Oss. Astronomico di Roma, Via Frascati 33, I-00040 Monteporzio (RM), Italy
[9] Dipartimento di Fisica e Scienze della Terra, Universitá degli Studi di Ferrara, via Saragat 1, I-44122 Ferrara, Italy
[10] IFPU - Inst. for Fundamental Physics of the Universe, Via Beirut 2, I-34014 Trieste, Italy

Abstract. We present the main results of the INAF/ASI project based on the *Chandra* Large Program (700 ks) on the Spiderweb Galaxy at z=2.16, one of the most intensively studied protocluster region. To date, this is the longest X-ray observation targeting a protocluster, and allowed us to i) measure an high fraction of active galactic nuclei among the protocluster member galaxies; ii) detect diffuse hot baryons within 80 kpc from the Spiderweb Galaxy center and investigate its relation with the formation of the proto-ICM; iii) characterize the interaction between the radio jets and the surrounding medium. This program is carried by an international team that includes PIs of proprietary data on the Spiderweb in the radio (JVLA) and sub-mm (ALMA) bands, which complement the X-ray data together with optical and NIR archival data. Within this project, we also explored the star formation in protocluster galaxies, the metallicity of the ICM, the co-evolution of the central SMBH with the host cluster, the ICM and the central galaxy, through intensive numerical simulations in a series of papers aimed at providing a coherent interpretative framework to the observations. In addition, we exploited the *Chandra* archive to map the iron distribution in the ICM of evolved clusters at $z < 1.2$, showing that the positive evolution with cosmic epoch is due to the accumulation of iron in the cluster cores, with a little increase in the iron total mass. Combining the scientific results of this project, allows us to make significant progress towards a comprehensive picture of the baryon cycle in groups, clusters and protoclusters of galaxies across cosmic epochs.

Key words. galaxies: clusters: general; intracluster medium – galaxies: active – X-rays: AGN – X-rays: galaxies: clusters

1. Introduction

The study of the formation of the first massive virialized halos has become one of the main quests for extragalactic astronomy. In particular, the thermodynamics of the intra-cluster medium (ICM) and the activity of the galaxy population in the so-called protoclusters at $z \sim 2$, offer a unique window on the transformation processes driven by the environment, that are expected to be significantly enhanced in dense cosmic regions. To date, few protoclusters have been studied in the X-ray band, despite this is the most efficient window to search for ICM and AGN. Available archival data provide only some hints of positive evolution with redshift of X-ray sources within clusters and protoclusters, but are not sufficient for a quantitative estimate on the AGN luminosity function, the ICM properties, and the environmental effects on the coevolution of galaxies and supermassive black holes (SMBH), including the brightest central galaxy (BCG).

Our *Chandra* Large Program of 700 ks on the remarkable Spiderweb Galaxy complex (PKS 1138262) at $z = 2.16$, provides a unique opportunity to address these key scientific questions. The region is surrounded by a 2 Mpc–sized overdensity of star forming galaxies (Ly_α and H_α emitters), dusty starbursts, and red galaxies in the process of shaping a nascent red sequence. This complex, embedded in a giant Ly_α halo (Pentericci et al. 1997; Miley et al. 2006), is considered a typical protocluster region which is expected to evolve into a massive cluster with virial mass $> 10^{14} M_\odot$ in less than 1.5 Gyr. The Spiderweb Galaxy complex has become an intensively studied region, with observations ranging from radio, to submm, IR, and optical wavelengths. Our deep, high resolution X-ray observation awarded in Chandra AO20 is key to detect and characterize the extended emission from the ICM, to obtain a comprehensive physical picture of the accretion onto SMBH, and to investigate the link between the vigorously starforming galaxies and their nuclear activity. Our unprecedented study of the Spiderweb constitutes a first step of a much broader project that includes also a detailed study of the iron distribution in the ICM of virialized clusters at $z < 1.2$ based on archival *Chandra* data, and intensive numerical simulations of groups and cluster of galaxies to interpret our observations on the effects of feedback and the thermodynamical evolution of the ICM. The final goal is to progress towards a complete and coherent picture of the baryon cycling in dense environments at cosmic epochs from the peak of star formation and SMBH accretion to the secular evolution at lower redshifts.

2. The AGN population and diffuse emission in the Spiderweb Protocluster

Our ACIS-S *Chandra* data provided an unprecedented deep view of the environment of a $z > 2$ protocluster within a radius of ~ 5 arcmin (2.5 Mpc) from the central galaxy. We identify unresolved X-ray sources in the field down to flux limits of 1.3×10^{-16} and 3.9×10^{-16} erg/s/cm^2 in the soft (0.5-2.0 keV) and hard (2-10 keV) band, respectively, detecting 107 X-ray unresolved sources, among which 13 have optical counterparts with spectroscopic redshift $2.11 < z < 2.20$, and 1 source with photometric redshift consistent with this range (see Figure 1). Our X-ray spectral analysis shows that their intrinsic spectral slope is consistent with an average $\langle \Gamma \rangle \sim 1.84 \pm 0.04$. Excluding the Spiderweb Galaxy, the best-fit intrinsic absorption for 5 protocluster X-ray members is $N_H > 10^{23}$ cm^{-2}, while other 6 have upper limits of the order of few$\times 10^{22}$ cm^{-2}. Two sources can only be fitted with very flat $\Gamma \leq 1$, and are therefore considered Compton-thick candidates. The 0.5-10 keV rest frame luminosities of the 11 Compton-thin protocluster members, corrected for intrinsic absorption, are greater than 2×10^{43} erg/s. These values are typical of Seyfert-like galaxies and significantly larger than X-ray luminosities expected from star formation. The X-ray luminosity function of AGN in the volume associated to the Spiderweb protocluster in the range $10^{43} < L_X < 10^{44.5}$ erg/s, is 5 times higher than in the field at the same redshift and significantly flatter, implying an increasing excess at the bright end (see Figure 2, top). The X-ray AGN fraction is mea-
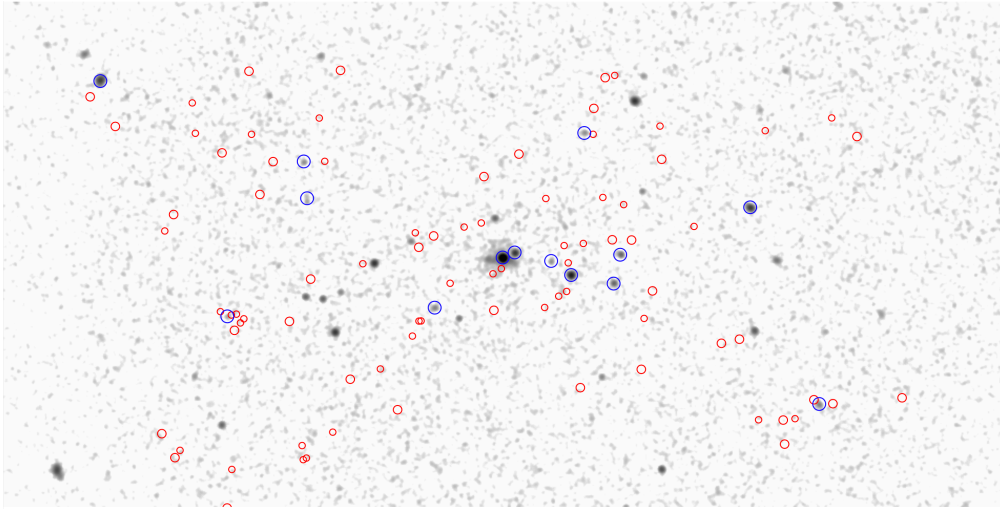
Fig. 1. Full band (0.5-7.0 keV) image of the center of the field (a box of 460×240 arcsec) with the X-ray emitting protocluster members marked with blue circles, and all the other spectroscopically confirmed protocluster members (2.0 < z < 2.3) marked with red circles. The image has been smoothed with a 1 arcsec Gaussian filter for clarity (from Tozzi et al. 2022, Paper I).

sured to be 25.5 ± 4.5% of the spectroscopically confirmed members in the estimated stellar mass range $\log(M_*/M_\odot) > 10.5$ (see Figure 2, bottom). This value corresponds to an AGN enhancement factor of $6.0^{+9.0}_{-3.0}$ with respect to the COSMOS field at comparable redshifts and stellar mass range. This puts the Spiderweb as the protocluster with the highest AGN fraction at $\log(M_*/M_\odot) > 10.5$ compared to the few objects studied in the literature with comparable data coverage (see Figure 2, bottom). These results are presented in Tozzi et al. (2022), where we conclude that the galaxy population in the Spiderweb Protocluster is characterized by enhanced X-ray nuclear activity triggered by environmental effects on Mpc scales.

Thanks to the exquisite angular resolution of *Chandra*, we obtained at the same time a robust characterization of the strong, unresolved nuclear emission, and of the extended emission within a radius of 12 arcsec from the Spiderweb Galaxy. We use the radio image of the jets obtained with the JVLA to identify the regions overlapping the radio emission (see Figure 3), and perform X-ray spectral analysis separately in the jet regions and in the complementary area. We find that the

Spiderweb galaxy hosts a mildly absorbed quasar, with a modest variability on a time scale of ~ 1 year. We find that the diffuse emission in the jet regions is significantly harder than the rest of the extended emission, and consistent with inverse-Compton upscattering of the CMB photons by the relativistic electrons. We also find a slightly asymmetric, diffuse emission within a radius of ~ 90 kpc from the Spiderweb Galaxy (Figure 4, top). This emission is very soft, and it is consistent with thermal emission from hot ICM with a temperature of ~ 2 keV (Figure 4, bottom), for a total ICM mass of $(1.67 \pm 0.17) \times 10^{12} M_\odot$, in agreement with the $L - T$ relation for massive clusters. We conclude that the Spiderweb Galaxy has a core of hot, diffuse baryons that may have been heated by gravitational shocks and/or by feedback-induced shocks.

3. Distribution and evolution of iron in the ICM at $z < 1.2$

We exploited the *Chandra* archive to perform spatially-resolved spectroscopy of the ICM of massive clusters at $z < 1.2$ to map the iron as a function of radius and redshift, and therefore
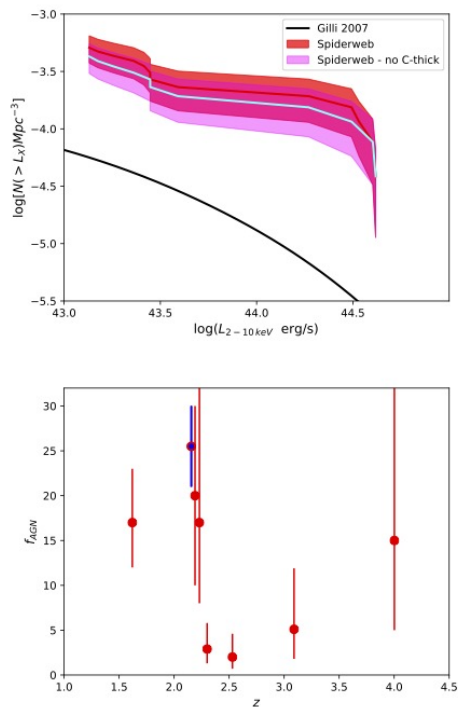
Fig. 3. Close-up of the Spiderweb Galaxy at full angular resolution, in the soft (0.5-2 keV) band. Extended emission is clearly visible. Red contours show radio emission observed in the 10 GHz band with the JVLA (see Carilli et al. 2022, in press) at levels of 0.03, 0.2, 2 and 20 mJy/beam (from Tozzi et al. 2022, Paper I).

Fig. 2. Top: the red, solid line with the red-shadowed area shows the cumulative rest-frame, hard-band luminosity function of the AGN in the protocluster (including and excluding the C-thick candidates), in the comoving volume defined by $2.11 < z < 2.20$ and a circle of 2.5 arcmin radius. The black solid line is the XLF in the field from the model of Gilli et al. (2007). Shaded areas correspond to 1σ uncertainty. Bottom: the fraction of X-ray AGN over the total number of identified protocluster members for the sample of protoclusters with deep X-ray data. The Spiderweb Protocluster is marked with a blue dot. Figures from Tozzi et al. 2022 (Paper I).

trace the effects of iron production and mixing across cosmic epochs. In Liu et al. (2018) we investigate the spatial distribution of iron in the intra-cluster medium in a selected sample of 41 relaxed clusters in the range $0.05 < z < 1.03$. We compute the azimuthally-averaged, deprojected Z_{Fe} profile of each cluster out to $\sim 0.4 r_{500}$, and identify a peak in the distribution of iron followed by a flatter distribution at larger radii. We quantify the extent of the iron
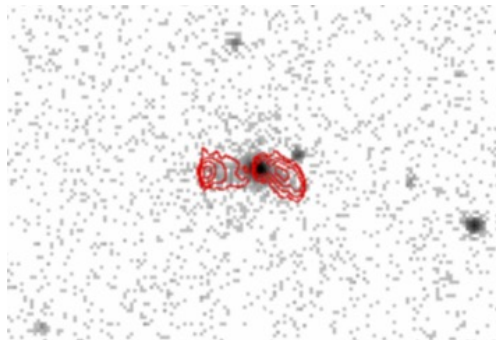
distribution in each cluster with a normalized scale parameter r_{Fe}, defined as the radius where the iron abundance excess is half of its peak value. We find that r_{Fe} increases by a factor of ~ 3 from $z \sim 1$ to $z \sim 0.1$, suggesting that the spatial distribution of iron in the ICM extends with time, possibly due to the mixing associated with the mechanical-mode feedback from the central galaxy. We also find that the iron mass excess within $0.3 r_{500}$, when normalized to the total baryonic mass in the same region, does not evolve significantly, showing that it is already established at $z \sim 1$.

In performing this analysis, we also addressed poorly-known processes, such as the depletion of Fe into dust grains in the central, high-density regions, which creates a central drop of ICM Fe abundance that has been observed in several cool-core clusters. Since noble gas elements such as Ar and Ne are not expected to be depleted into dust, and therefore should not show any drop, we test the depletion scenario by measuring with *Chandra* data the radial profiles of Ar and Ne in a sample of 12 groups and clusters where a central drop in Fe abundance has been detected (Liu et al. 2019). Our results depict a scenario in which some fraction of Fe is depleted into dust grains in the inner regions, although the global central abundance drop is mostly due to mechan-
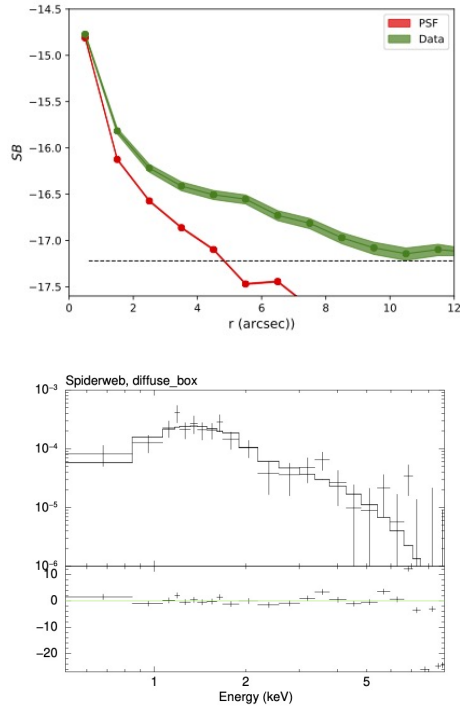
Fig. 4. Top: the profile of the AGN simulated image (red) compared to the Spiderweb profile (line) in the soft band, which is dominated by the thermal, isotropic emission detected outside the jet regions. The horizontal line shows the instrumental plus unresolved X-ray background level. Bottom: folded spectrum of the emission in the diffuse region outside the jets fitted with a thermal `mekal` model plus the AGN contamination (from Tozzi et al. 2022, Paper II).

Fig. 5. *Top*: the dependence of $Z_{\mathrm{Fe}}^{\mathrm{peak}}$ and $Z_{\mathrm{Fe}}^{\mathrm{plateau}}$ on redshift as described by the best-fit power-law $X = n \cdot (1 + z)^{-\gamma}$, with its 1σ uncertainty. *Bottom*: the dependence of $M_{\mathrm{Fe}}^{\mathrm{peak}}/M_{\mathrm{gas}}$ and $M_{\mathrm{Fe}}^{\mathrm{plateau}}/M_{\mathrm{gas}}$ on redshift. These two plots represent a synthetic description of the cosmic evolution of the iron abundance obtained in Liu et al. (2020).

ical processes, like the displacement of metal-rich ICM from the very center to larger radii by AGN-driven feedback.

Finally, in Liu et al. (2020), we study the chemical evolution of galaxy clusters by measuring the iron mass in the ICM after dissecting the abundance profiles into different components. We used Chandra archival observations of 186 morphologically regular clusters in the redshift range of [0.04, 1.07]. For each cluster, we computed the azimuthally averaged iron abundance and gas density profiles. In par-
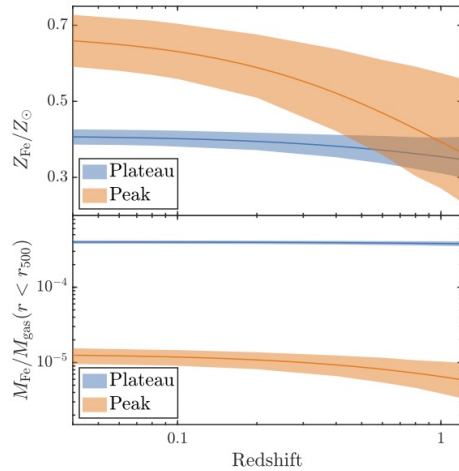
ticular, our aim is to identify a central peak in the iron distribution, which is associated with the central galaxy, and an approximately constant plateau reaching the largest observed radii, which is possibly associated with early enrichment that occurred before or shortly after achieving virialization within the cluster. We were able to firmly identify two components in the iron distribution in a significant fraction of the sample simply by relying on the fit of the iron abundance profile. We find that the iron plateau shows no evolution with redshift. On the other hand, we find a marginal ($< 2\sigma$ c.l.) decrease with redshift in the iron mass included in the iron peak rescaled by the gas mass. We measure that the fraction of iron-peak mass is typically a few percent ($\sim 1\%$) of the total iron mass within r500. Therefore, since the total iron mass budget is dominated by the plateau, we find consistently that the global gas mass-weighted iron abundance does
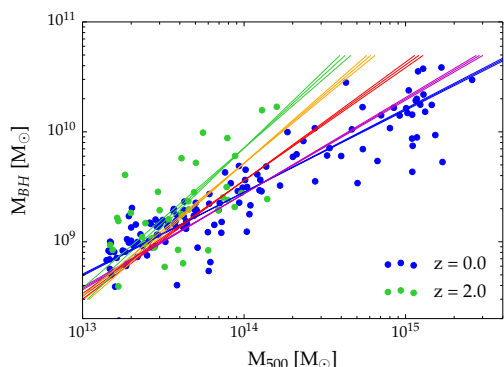
Fig. 6. Correlation between M_{BH} and M_{500} at different redshifts. Namely, we show in green, orange, red, magenta, and blue the mass sample related to $z = 2, 1.5, 1, 0.5$ and 0, respectively. Figure from Bassini et al. (2019).

Fig. 7. SFR of protocluster regions at $z \sim 2$ in observations and simulations within an aperture of ~ 2 pMpc. Blue squares refer to the Spiderweb structure (Dannerbauer et al. 2014). Green square and green band refer to the two protoclusters analysed by Kato et al. (2016, HS1700 and 2QZCluster respectively), while red bands are from Clements et al. (2014), and black solid lines from Stevens et al. (2010). Black circles and triangles refer to numerical simulations, where the SFR is plotted against protocluster mass (Bassini et al. 2020).

not evolve significantly across our sample. We were also able to reproduce past claims of evolution in the global iron abundance, which turn out to be due to the use of cluster samples with different selection methods combined with the use of emission-weighted, instead of gas mass-weighted, abundance values. Finally, while the intrinsic scatter in the iron plateau mass is consistent with zero, the iron peak mass exhibits a large scatter, in line with the fact that the peak is produced after the virialization of the halo and depends on the formation history of the hosting cool core and the strength of the associated feedback processes. Thanks to our spatially resolved approach, we settled the issue of iron abundance evolution in the ICM, reconciling the contradictory results obtained in the last ten years. The path towards a full and comprehensive chemical history of the ICM requires the application of high angular resolution X-ray bolometers and a dramatic increase in the number of faint, extended X-ray sources.

4. Star formation and ICM in clusters and protoclusters explored with numerical simulations

Cosmological hydrodynamical simulations of a large sample of simulated objects, from poor groups to rich clusters, provide support to the
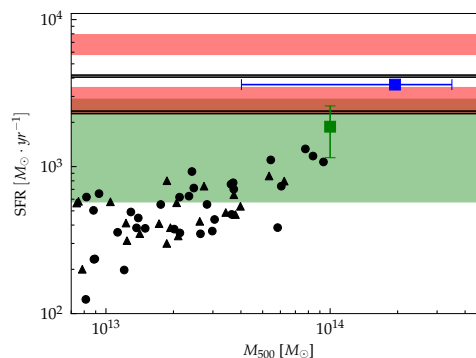
interpretation of the halo mass - iron abundance (and metallicity) relation. In Truong et al. (2019) we perform simulations with an improved version of the smoothed-particle-hydrodynamic GADGET-3 code and consider various astrophysical processes including radiative cooling, metal enrichment and feedback from stars and AGN. The scaling between the metallicity and the temperature obtained in the simulations agrees well in trend and evolution with the observations. We find that the iron abundance in the cluster core ($r < 0.1 R_{500}$) does not correlate with the temperature nor presents a significant evolution. The scale invariance is confirmed when the ICM metallicity is related directly to the total mass. We also investigate the impact of the AGN feedback and find that it plays a key role in producing a flat metallicity distribution in the outskirts of all systems, from groups to clusters, providing support to the picture of early enrichment.

The correlations between the mass of the SMBH in the BCG and cluster mass and temperature are investigated with simulations in

Bassini et al. (2019). We focus on 135 groups and clusters with a mass range $1.4 \times 10^{13} M_\odot -$ $2.5 \times 10^{15} M_\odot$ extracted from a set of 29 zoom-in cosmological hydro-dynamical simulations where the baryonic physics is treated with various sub-grid models, including feedback by AGN. We find that the BH mass correlates with M_{500} and T_{500}, and that the MBH - M_{500} relation evolves with time, becoming shallower at lower redshift as a direct consequence of hierarchical structure formation (see Figure 6). On average, the contribution of gas accretion to the total SMBH mass dominates for the majority of the cosmic time ($z > 0.4$), while in the last 2 Gyr the BH-BH mergers become a larger contributor. Our results also imply that clusters temperature and mass can be a useful proxy for the SMBHs mass, especially at high redshift.

Finally, in Bassini et al. (2020) we studied the star formation rate (SFR) in the same cosmological hydrodynamical simulations of galaxy clusters and proto-clusters in the redshift range $0 < z < 4$, comparing them to recent observational studies. We find that values of SFR are under predicted in protocluster cores by a factor ≥ 4 both at $z \sim 2$ and $z \sim 4$ (see Figure 7), as a direct consequence of the under prediction of the normalisation of the main sequence of SF galaxies by a factor of ~ 3, which it is probably due to the under prediction of the gas mass fraction and star formation efficiency. We observed that the current subgrid model for star formation is not suitable to describe violent events like high-redshift starbursts which cannot be reproduced in simulations by merely changing the SF model parameters. The increasing number of multi-wavelength, high-redshift observations will help to improve the current star formation model, which is needed to fully recover the observed star formation history of galaxy clusters.

5. New lines of research: ICM bulk motions, and X-ray lensing

As a byproduct of our studies on the iron emission line system in X-ray spectra of the ICM, we investigate the bulk motion of the ICM of clusters in non-equilibrium dynamical config-

uration. We find a peculiar signature, possibly related to global rotation of the ICM, in the galaxy cluster Abell 2107, where previous studies detected rotational motion in the member galaxies with a high significance level. By fitting the centroid of the iron K_α line complex at 6.7–6.9 keV rest frame in *Chandra* spectra, we find a gradient as a function of the projected distance from the identified rotation axis, compatible with a rotation pattern with maximum tangential velocity $v_{max} = 1380 \pm 600$ km/s at a radius $\lambda_0 \sim 160$ kpc. This result, if interpreted in the framework of hydrostatic equilibrium, as suggested by the regular morphology of Abell 2107, would imply a large mass correction of the order of $\Delta M = (6 \pm 4) \times 10^{13} M_\odot$ at ~ 160 kpc, and, in turn, an oblate shape that is incompatible with the cluster morphology itself, which appears to be almost spherical. A more conservative interpretation may be provided by an unnoticed off-center, head-on collision between two comparable halos. Our analysis confirms that ICM dynamics are a key ingredient to derive hydrostatic mass in clusters, a science case that can be addressed by the next-generation X-ray facilities carrying X-ray bolometers onboard.

Combining our expertise with both extended and unresolved X-ray emission, we exploit the high angular resolution of *Chandra* to search for unresolved X-ray emission from lensed sources in the field of view of 11 CLASH clusters, whose critical lines and amplification maps have been previously obtained by accurate strong lensing models. Our main goal is to assess the efficiency of massive clusters as cosmic telescopes to explore the faint end of the X-ray extragalactic source population. We detect X-ray emission, either in the soft (0.5–2 keV) or hard (2–7 keV) band, only in 9 out of 849 lensed/background optical sources. Based on the untargeted detection in the soft, hard and total band images, we find 66 additional X-ray sources with no spectroscopic confirmation, that are consistent with being lensed (background) sources. Assuming an average redshift distribution consistent with the Chandra Deep Field South survey (CDFS), we estimate their magnification and measure for the first time the soft- and hard-band num-

ber counts of lensed X-ray sources. The results are consistent with current modelization of the AGN population distribution. In terms of depth, the distribution of de-lensed fluxes of the sources identified in moderately deep CLASH fields reaches a flux limit of $\sim 10^{-16}$ and $\sim 10^{-15}$ erg/s/cm^2 in the soft and hard bands, respectively, therefore approximately 1.5 order of magnitudes above the flux limit of the CDFS. We conclude that, in order to match the depth of the CDFS exploiting massive clusters as cosmic telescopes, the required number of massive cluster fields is about two orders of magnitude larger than that offered by targeted high-mass clusters in the Chandra archive. At the same time, the discovery of strongly lensed sources close to the critical lines remains an attractive, albeit rare occurrence, due to the low source density in the X-ray sky. In addition, systematic search for the more frequent AGN-galaxy and AGN-group lensing, may provide significantly higher statistics once high-resolution, wide area X-ray surveys will be available. Therefore, future X-ray facilities, with ~ 1 arcsec angular resolution and large effective area, will fully exploit the potential of X-ray lensing, including the study of faint AGN activity in the early Universe and the measurement of gravitational time delays through X-ray variability of multiply imaged AGN.

6. Conclusions

The project "Mapping Feedback Processes in the protoIntracluster Medium", funded by ASI/INAF contract in 2019, in two years achieved significant results unveiling environmental effects on protocluster galaxies, radio jet/ICM interactions, and the presence of hot diffuse baryons in the remarkable Spiderweb Galaxy complex. We also adopted a complementary approach to investigate the evolution of the diffuse baryons in groups and cluster, in particular the dependence on position and epoch of the iron distribution, as a tracer of the combined effect of the stellar and nuclear feedback. Finally, we extensively analyzed hydrodynamical simulations to interpret the observa-

tions in terms of physical processes. This work paved the way for deep studies of protoclusters at $z \geq 2$, where feedback and environmental processes drive a rapid evolution in the galaxy population, particularly in the central brightest galaxy, shedding light on physical phenomena that are believed to affect all the galaxies at some point during their evolution.

References

Bassini, L., Rasia, E., Borgani, S., et al. 2020, A&A, 642, A37

Bassini, L., Rasia, E., Borgani, S., et al. 2019, A&A, 630, A144

Clements, D. L., Braglia, F. G., Hyde, A. K., et al. 2014, MNRAS, 439, 1193

Dannerbauer, H., Kurk, J. D., De Breuck, C., et al. 2014, A&A, 570, A55

Gilli, R., Comastri, A., & Hasinger, G. 2007, A&A, 463, 79

Kato, Y., Matsuda, Y., Smail, I., et al. 2016, MNRAS, 460, 3861

Liu, A., Tozzi, P., Ettori, S., et al. 2020, A&A, 637, A58

Liu, A., Tozzi, P., Yu, H., De Grandi, S., & Ettori, S. 2018, MNRAS, 481, 361

Liu, A., Zhai, M., & Tozzi, P. 2019, MNRAS, 485, 1651

Miley, G. K., Overzier, R. A., Zirm, A. W., et al. 2006, ApJ, 650, L29

Pentericci, L., Roettgering, H. J. A., Miley, G. K., Carilli, C. L., & McCarthy, P. 1997, A&A, 326, 580

Stevens, J. A., Jarvis, M. J., Coppin, K. E. K., et al. 2010, MNRAS, 405, 2623

Truong, N., Rasia, E., Biffi, V., et al. 2019, MNRAS, 484, 2896